JTTEE5 4:358-366

Numerical Simulation of Gas and Particle Flow in a High-Velocity Oxygen-Fuel (HVOF) Torch

C.H. Chang and R.L. Moore

A transient two-dimensional numerical simulation of Inconel spraying in a high-velocity oxygen-fuel (HVOF) torch barrel was performed. The gas flow is treated as a continuum multicomponent chemically reacting flow, whereas particles are modeled using a stochastic particle spray model, fully coupled to the gas flow. The calculated results agree well with experimental data and show important statistical aspects of particle flow in the torch.

Nomenclature

A_p	Particle surface ares (m^2)	$\mathbf{P}$	Momentum (kg·m/s)
$A_{\|\|}$	Projected surface area (m^2)	$P_{\|\|}$	Component of $\mathbf{P}$ parallel to wall (kg·m/s)
C_D	Drag coefficient	Pr_t	Turbulent Prandtl number
c	Total molar concentration (mole m^{-3})	p	Pressure (N/m^2)
c_{vs}	Solid specific heat (J/kg/K)	$\mathbf{q}$	Heat flux ($J/m^2/s$)
c_{vl}	Liquid specific heat (J/kg/K)	Re	Reynolds number
D_p	Particle diameter (m)	Sc_t	Turbulent Schmidt number
E_p	Particle internal energy (J)	T	Temperature (K)
e	Total thermal internal energy per unit mass (J/kg)	T_m	Melting temperature (K)
e_m	Specific energy of solid at T_m (J/kg)	T_p	Particle temperature (K)
e_p	Specific energy of particle (J/kg)	t	Time (s)
$\mathbf{F}_p$	Drag force ($kg \cdot m/s^2$)	$\mathbf{t}$	Unit vector parallel to wall
$\Delta_f H_i^0$	Heat of formation of species i at absolute zero (J/kg)	U	Component of $\mathbf{u}$ parallel to wall (m/s)
h	Heat transfer coefficient ($J/m^2/K/s$)	u	x component of $\mathbf{u}$ (m/s)
h_i	Specific enthalpy of species i (J/kg)	$\mathbf{u}$	Fluid velocity (m/s)
$\mathbf{I}$	Unit dyadic	$\mathbf{u}_p$	Particle velocity (m/s)
$\mathbf{i}$	Unit vector in x direction	V	Inflow velocity (m/s)
$\mathbf{j}$	Unit vector in y direction	V_{cell}	Volume of computational cell (m^3)
K	Thermal conductivity (J/m/K/s)	v	y component of $\mathbf{u}$ (m/s)
k	Turbulent kinetic energy per unit mass (m^2/s^2)	x	Radial coordinate (m)
L	Latent heat of fusion (J/kg)	x_i	Mole fraction of species i
M_i	Molecular weight	$\mathbf{x}_p$	Particle position (m)
$\dot{M}$	Mass flow rate (kg/s)	y	Axial coordinate (m)
m_p	Particle mass (kg)		

Greek Symbols

α	Fluid volume fraction	ρ	Total mass density (kg/m^3)
ε	Dissipation rate of turbulent kinetic energy (m^2/s^3)	ρ_i	Partial mass density of species i (kg/m^3)
ε_p	Surface emissivity of particle	σ	Stefan-Boltzmann constant ($J/m^2/K^4/s$)
η	Efficiency	τ	Shear stress ($kg/m/s^2$)
λ	Second viscosity coefficient (kg/m/s)	Φ	Viscous dissipation ($kg/m/s^3$)
μ	Viscosity (kg/m/s)	χ	Particle degree of melting
ν	Kinematic viscosity (m^2/s)		

Subscripts

D	Derriere (back) cell face	p	Particle
F	Front cell face	R	Right cell face
f	Gas around particle	t	Turbulence
L	Left cell face	w	Wall

Superscripts

T	Transpose

1. Introduction

HIGH-VELOCITY oxygen fuel (HVOF) spray techniques for producing high-performance metallic coatings have been used for over ten years. Many parametric studies have been performed on process controlling parameters and coating quality without a detailed understanding of the physical and chemical processes involved, especially in the presence of entrained particles. HVOF spraying involves an intricate interplay between fluid flow, heat transfer, turbulence, chemical reactions, diffusion of multicomponent gases, and various gas-particle interactions at elevated temperatures. A detailed understanding of these processes is essential for the HVOF process to reach its full potential.

Most modeling studies of HVOF systems have been limited to simple models for both flow and particle characteristics (Ref 1). Recently, however, Power et al. (Ref 2) used computational fluid dynamics (CFD) methods for detailed modeling of a HVOF system (METCO DJ gun from Metco, Westbury, NY 11590). This work was later applied to model particle flow in the system (Ref 3). However, their approach neglected particle effects on the gas flow, which were assumed to be steady in the presence of particles.

This paper presents a detailed transient numerical simulation of chemically reacting flow and its interaction with entrained particles in a commercial HVOF spray torch Hobart-Tafa JP-5000 (Hobart-Tafa Technologies, Inc., Concord, NH). Figure 1 shows a schematic diagram of the torch. Oxygen and fuel (kerosene) are injected into the combustion chamber, and the combustion products are accelerated in the converging-diverging nozzle. Particles are injected through the injection hole located downstream of the nozzle and are heated and accelerated in the barrel. This mixture of gas and particles is then discharged outside the torch toward the substrate located some distance from the barrel exit. The free jet outside the torch is not included in the present simulation because diagnostic results obtained by Swank et al. (Ref 4) showed that most particle heating and acceleration occur in the barrel. The combustion chamber also is not included for simplicity. The combustion chamber exit conditions are determined by equilibrium conditions, assuming complete combustion of the fuel.

Our model for gas-particle flows is based on a fluid-particle technique similar to that previously used to model fuel sprays in internal combustion engines (Ref 5, 6). The gas is represented as a continuous multicomponent chemically reacting ideal gas with temperature-dependent thermodynamic and transport properties (Ref 7). The particles are modeled as discrete Lagrangian entities that exchange mass, momentum, and energy with the gas. The model in its present form can simulate particle injection, heating, and melting, but not evaporation and condensation. Computational particles are stochastically generated by sampling from probability distributions of particle properties (size, velocity, etc.) at the point of injection (Ref 5, 6, 8). Each computational particle represents a group of similar physical particles. Particle trajectories and thermal histories are then calculated simultaneously with the motion of the gas. All gas-particle interactions are treated in a fully self-consistent manner, including turbulent dispersion of particles.

Keywords gas-particle interactions, HVOF, modeling, multicomponent flow

C.H. Chang and **R.L. Moore,** Idaho National Engineering Laboratory, Idaho Falls, ID 83415, USA.

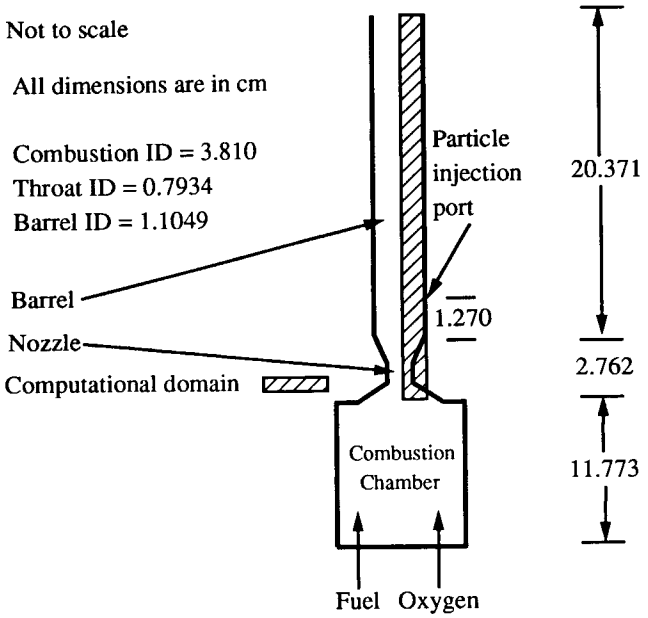

Fig. 1 Schematic of the HVOF torch used

The entire system of governing equations described above constitutes a comprehensive computational model for thermal spray systems. This model is embodied in the LAVA computer code (Ref 7), which has previously been applied to simulate plasma spraying (Ref 8) and various thermal plasma flows (Ref 9-11). The curved geometry of the converging-diverging nozzle is represented by the use of an excluded volume or porosity function to represent the fraction of each cell volume and cell face area that is available to the flow (Ref 12-14).

2. Computational Model

2.1 *Fluid Dynamical Model*

The fluid dynamical equations solved by LAVA consist of momentum and thermal internal energy equations for the multicomponent fluid mixture, continuity equations for each component of the mixture, and state and constitutive relations. Viscous stresses and thermal conduction are included in full generality, whereas species diffusion is represented by a self-consistent effective binary diffusion approximation (Ref 15).

The governing equations in LAVA are written in a form that includes two-dimensional (2-D) rectangular and cylindrical coordinates and three-dimensional (3-D) rectangular coordinates as special cases (Ref 7). The spatial coordinates are (x, y) in 2-D and (x, y, z) in 3-D. Here the flow is axisymmetric so that x is the radial coordinate, y is the axial coordinate, and $x = 0$ is the symmetry axis. In order to combine the rectangular and cylindrical cases, a geometrical variable, R, is introduced (Ref 7). Flow blockages in the domain may be represented by redefining R to include the volume available to the fluid (Ref 14):

$$R = \begin{cases} \alpha & \text{in 2–D or 3–D rectangular coordinates} \\ x\alpha & \text{in 2–D cylindrical coordinates} \end{cases} \quad \text{(Eq 1)}$$

The equations are written in terms of vectors and matrices in 2-D and 3-D Euclidean space for compactness as described previously (Ref 7, 14). In rectangular coordinates, these Euclidean vectors and matrices are isomorphic to the corresponding vectors and tensors in physical space. In the 2-D cylindrical case, however, it is essential to distinguish between the Euclidean quantities and the corresponding physical ones because cylindrical terms (e.g., centrifugal and Coriolis forces) and factors of R appear explicitly in the present Euclidean notation, whereas they are implicit in the customary physical vector-tensor notation (Ref 7, 14).

The species conservation equations are given by (Ref 7, 14):

$$\frac{\partial(R\rho_i)}{\partial t} + \nabla \cdot (R\rho_i \mathbf{u}) = -\nabla \cdot (R\mathbf{J}_i) + R\dot{\rho}_i^c \quad \text{(Eq 2)}$$

$$\frac{\partial(R\rho)}{\partial t} + \nabla \cdot (R\rho \mathbf{u}) = 0 \quad \text{(Eq 3)}$$

where the diffusion flux $\mathbf{J}_i$ of species i is given by a self-consistent effective binary diffusion approximation (Ref 7, 15), and $\dot{\rho}_i^c$ is the rate of change of ρ_i due to chemical reactions.

The momentum equation takes the form:

$$\frac{\partial(R\rho\mathbf{u})}{\partial t} + \nabla \cdot (R\rho\mathbf{u}\mathbf{u}) = -R\nabla\left(p + \frac{2}{3}\rho k\right) + \nabla \cdot (R\sigma) - \sigma_0 \nabla R - \frac{R}{x}\sigma_1 \nabla x + R\mathbf{F} \quad \text{(Eq 4)}$$

where $\mathbf{F}$ is the momentum source/sink due to entrained particles (defined later). The viscous stresses are given by (Ref 13, 14):

$$\sigma = (\mu + \mu_t)[\nabla\mathbf{u} + (\nabla\mathbf{u})^{\mathrm{T}}] + (\lambda + \lambda_t)D\mathbf{I} \quad \text{(Eq 5)}$$

$$\sigma_0 = \frac{2(\mu + \mu_t)}{R}\mathbf{u} \quad \nabla R - \frac{2(\mu + \mu_t)}{x}\mathbf{u} \cdot \nabla x + (\lambda + \lambda_t)D \quad \text{(Eq 6)}$$

$$\sigma_1 = 2(\mu + \mu_t)\left(\frac{2}{x}\mathbf{u} \cdot \nabla x - \frac{1}{R}\mathbf{u} \cdot \nabla R\right) \quad \text{(Eq 7)}$$

where μ_t is the turbulent viscosity (defined later), $\lambda_t = -(2/3)\mu_t$, and $D = R^{-1}\nabla \cdot (R\mathbf{u})$.

The thermal internal energy equation is given by (Ref 7, 14):

$$\frac{\partial(R\rho e)}{\partial t} + \nabla \cdot (R\rho e\mathbf{u}) = -p\nabla \cdot (R\mathbf{u}) - \nabla \cdot (R\mathbf{q}) + R\rho\varepsilon + R\dot{Q}^c + R\dot{Q} \quad \text{(Eq 8)}$$

where $\dot{Q}^c$ is the rate of change of ρe due to chemical reactions (Ref 7), and $\dot{Q}$ is the heat source/sink due to injected particles (defined later). In the present simulation, the radiation loss has been neglected. The heat flux vector $\mathbf{q}$ contains contributions from both pure heat conduction and species diffusion (Ref 7). The temperature is obtained by general thermodynamic state relations for multicomponent mixtures (Ref 7). In laminar flow $\rho\varepsilon = \Phi$, where:

$$\Phi = \sigma : \nabla\mathbf{u} + \frac{\sigma_0}{R}\mathbf{u} \cdot \nabla R + \frac{\sigma_1}{x}\mathbf{u} \cdot \nabla x \quad \text{(Eq 9)}$$

In the present simulations, the k-ε turbulence model (Ref 7) is used to represent the effects of turbulence. Transport equations are solved for k and ε,

$$\frac{\partial(R\rho k)}{\partial t} + \nabla \cdot (R\rho k\mathbf{u}) = -\frac{2}{3}\rho k\nabla \cdot (R\mathbf{u}) + \nabla \cdot [R(\mu + \mu_t)\nabla k] + R\Phi - R\rho\varepsilon + R\dot{W} \quad \text{(Eq 10)}$$

$$\frac{\partial(R\rho\varepsilon)}{\partial t} + \nabla \cdot (R\rho\varepsilon\mathbf{u}) = \left(c_3 - \frac{2}{3}c_1\right)\rho\varepsilon\nabla \cdot (R\mathbf{u}) + \nabla \cdot \left[R\left(\mu + \frac{\mu_t}{\sigma_\varepsilon}\right)\nabla\varepsilon\right] + \frac{R\varepsilon}{k}(c_1\Phi - c_2\rho\varepsilon + c_s\dot{W}) \quad \text{(Eq 11)}$$

where the coefficients are given by $c_1 = 1.44$, $c_2 = 1.92$, $c_3 = -1.0$, $\sigma_\varepsilon = 1.3$, and $c_s = 1.5$ (Ref 6), and $\dot{W}$ represents the source/sink due to the interaction with particles, which is defined later. The turbulent viscosity, μ_t, is then given by:

$$\mu_t = \frac{c_\mu \rho k^2}{\varepsilon} \quad \text{(Eq 12)}$$

where $c_\mu = 0.09$. This is the same version of the k-ε model described and used in previous studies (Ref 7, 9), with the same values of the various parameters. In particular, we use the values $\mathrm{Pr_t} = \mathrm{Sc_t} = 0.7$ instead of the more conventional values $\mathrm{Pr_t} = \mathrm{Sc_t} = 0.9$.

Simple k-ε models of this type are not really satisfactory even for simple incompressible flows, for which they often require ad hoc corrections. However, such models usually do provide useful semiquantitative results of fair accuracy (Ref 9, 10), and one may reasonably hope that this will continue to be the case in simulations of the present type.

2.2 *Particle Model*

The particles are modeled by a stochastic discrete-particle model (Ref 8). Each computational particle, p, represents a number, N_p, of similar physical particles. The equations of motion of the particles are (Ref 8):

$$\frac{d\mathbf{x}_p}{dt} = \mathbf{u}_p \quad \text{(Eq 13)}$$

$$m_p \frac{d\mathbf{u}_p}{dt} = \mathbf{F}_p = C_D \frac{\pi D_p^2}{8} \rho_f |\mathbf{u}_f + \mathbf{u}_p' - \mathbf{u}_p| (\mathbf{u}_f + \mathbf{u}_p' - \mathbf{u}_p)$$

(Eq 14)

where $\mathbf{u}_p'$ is the turbulent velocity fluctuation that the particle, p, sees when time step Δt is less than the turbulent time scale (Ref 5, 6). When Δt is larger than the turbulent time scale, the particle position and velocity are updated by sampling from appropriate probability distributions (Ref 5, 6).

The particle energy equation is:

$$\frac{dE_p}{dt} = A_p [h(T_f - T_p) - Q_r] \quad \text{(Eq 15)}$$

where $\dot{Q}_r = \sigma\varepsilon_p (T_p^4 - T_w^4)$ is the rate of radiation heat loss from the particle surface. Here, T_w, ε_p, and σ are the wall temperature, surface emissivity, and Stefan-Boltzmann constant, respectively. The drag and heat transfer coefficients are obtained from Ref 6. The equation of state of the particle is $T_p(e_p)$, where $e_p = E_p/m_p$ and T_p is assumed to have the form:

$$T_p(e) = \begin{cases} (1/c_{vs})e_p & (e_p \le e_m) \\ T_m & (e_m < e_p \le e_m + L) \\ T_m + (1/c_{vl})(e_p - e_m - L) & (e_p > e_m + L) \end{cases}$$

(Eq 16)

In this formulation melting is automatically taken into account and requires no special logic. The degree of melting of a partially molten particle is simply $\chi = (e_p - e_m)/L$.

The exchange terms $\mathbf{F}_p$ and $A_p h(T_f - T_p)$ must also appear with the opposite sign in the fluid dynamical equations for the gas. For this purpose, it is necessary to sum over all particles in the appropriate computational cell. Thus we define the cell quantities:

$$\mathbf{F} = -\frac{1}{\alpha V_{cell}} \sum_p N_p \mathbf{F}_p \quad \text{(Eq 17)}$$

$$\dot{Q} = \frac{1}{\alpha V_{cell}} \sum_p N_p [A_p h(T_p - T_f) + \mathbf{F}_p \cdot (\mathbf{u}_f + \mathbf{u}_p' - \mathbf{u}_p)]$$

(Eq 18)

$$\dot{W} = -\frac{1}{\alpha V_{cell}} \sum_p N_p \mathbf{F}_p \cdot \mathbf{u}_p' \quad \text{(Eq 19)}$$

2.3 *Chemical Reactions*

Chemical reactions in the combustion products flowing through the converging-diverging nozzle and the barrel are included in the present simulation. We assumed that the combustion of the fuel ($C_{10}H_{20}$) is complete in the combustion chamber, and no unburned hydrocarbons are present in the mixture. Species present in the mixture are determined by an equilibrium chemistry analysis (Ref 16) of the stoichiometric mixture of the fuel and O_2 (15 moles of oxygen per mole of fuel). The mole fractions of the species in equilibrium at various temperatures at atmospheric pressure are shown in Table 1. Changes in pressure have very small effects on composition. We included all of the species in Table 1, except for HO_2, which is negligible over the entire temperature range of interest in this study.

Table 1 Mole fractions at various temperatures for the mixture of one mole of $C_{10}H_{20}$ and 15 mole of O_2

	1000 K	1500 K	2000 K	2500 K	3000 K	3500 K
CO	0.00000	0.00021	0.00898	0.07428	0.20784	0.25765
CO_2	0.50000	0.49972	0.48802	0.39945	0.19831	0.05150
H	0.00000	0.00000	0.00007	0.00293	0.03314	0.15267
HO_2	0.00000	0.00000	0.00000	0.00000	0.00002	0.00003
H_2	0.00000	0.00008	0.00201	0.01371	0.04459	0.06768
H_2O	0.50000	0.49983	0.49408	0.44870	0.30694	0.10816
O	0.00000	0.00000	0.00005	0.00282	0.03521	0.15214
OH	0.00000	0.00003	0.00175	0.01973	0.07607	0.11390
O_2	0.00000	0.00014	0.00505	0.03838	0.09786	0.09627

The chemical reactions included are:

$$\begin{aligned} H + H + M &\leftrightarrow H_2 + M \\ H + OH + M &\leftrightarrow H_2O + M \\ H + O + M &\leftrightarrow OH + M \\ O + O + M &\leftrightarrow O_2 + M \\ CO + O + M &\leftrightarrow CO_2 + M \\ H + O_2 &\leftrightarrow OH + O \\ H_2 + O &\leftrightarrow OH + H \\ H_2O + O &\leftrightarrow 2OH \\ H_2 + OH &\leftrightarrow H_2O + H \\ CO + OH &\leftrightarrow CO_2 + H \\ CO_2 + O &\leftrightarrow CO + O_2 \end{aligned}$$

where M denotes the third body. The first five slow reactions involving third bodies are treated by a conventional linearly implicit kinetic chemistry routine (Ref 7), and the remaining six fast reactions are treated kinetically by a newly developed, fully implicit chemistry routine for treating an arbitrary system of coupled fast and slow chemical reactions in fluid dynamics (Ref 17). The reaction rate coefficients, equilibrium constants, and third body efficiencies are obtained from published rate data (Ref 18, 19).

3. Calculation Domain and Boundary Conditions

The computational region is the converging-diverging nozzle and the straight barrel as illustrated in Fig. 1 and is subdivided by a nonuniform 21 by 198 computational mesh. The left boundary is the symmetry axis, and the flow is upward. The top boundary is the open boundary, which is an outflow boundary in this particular simulation. The right boundary is the barrel wall, and the "law of the wall" (described later) is used for the boundary conditions. The bottom boundary is the inflow boundary, whose properties are determined by the throat choke condition and chemical equilibrium as explained below.

3.1 *Inflow Conditions*

Simulations of this type require detailed fluid properties at the inflow, such as temperature, species concentrations, and velocity. In the present case, however, the properties of flow from the combustion chamber are not precisely known. Therefore, the inflow conditions are obtained from the given torch operating conditions, nozzle geometry, and the assumption of complete combustion and chemical equilibrium as described below.

The total mass flow rate $\dot{M}$ is simply obtained by the fuel and oxygen flow rate of the torch as:

$$\dot{M} = \dot{M}_{\text{fuel}} + \dot{M}_{O_2} \qquad \text{(Eq 20)}$$

The net energy input to the gas $\dot{H}$ is determined by:

$$\dot{H} = \eta \sum_i \dot{M}_i \left(h_i (T_{\text{in}}) + \frac{\Delta_f H_i^0}{M_i} \right) \quad (i = \text{fuel}, O_2) \qquad \text{(Eq 21)}$$

where $\dot{M}_i$ is the mass flow rate of species i, T_{in} is the temperature of the fuel and oxygen supplied to the torch, which is 300 K, and η is the efficiency of the combustion chamber, which is set to 0.8 for the present calculation (i.e., 20% heat loss to the cooling water, Ref 20).

The species densities at the inflow are determined from the chemical equilibrium conditions at the given temperature, pressure, and the elemental composition of the fuel-oxygen mixture. The chemical equilibrium conditions and equilibrium constant relations results in a set of nonlinear equations that are solved iteratively using Newton's method. These equations actually determine only mole fraction ratios, from which absolute molar concentrations are obtained using the equation of state.

In summary, species densities, temperature, velocity, and pressure at the inflow boundary are determined by $\dot{M}$, $\dot{H}$, and the throat condition of the converging-diverging nozzle by an iterative procedure for each time step:

1. Guess temperature and pressure for inflow.
2. Obtain species densities ρ_i using chemical equilibrium conditions.
3. Determine the inflow velocity V from the mass conservation conditions $\Sigma_i \rho_i AV = \dot{M}$.
4. Find the temperature from the total specific enthalpy of the combustion products using:

$$\dot{H} = \sum_i \rho_i \left(h_i(T) + \frac{\Delta_f H_i^0}{M_i} + \frac{1}{2} V^2 \right) AV \qquad \text{(Eq 22)}$$

5. Iterate until a converged temperature is obtained.

The radial component of inflow velocity is assumed to be zero.

The preceding procedure produces a unique solution for the guessed pressure. The pressure at the inflow is determined by an adaptive procedure from the choking condition. Initially, the pressure at the inflow boundary needs to be guessed. From the next cycle, the pressure at the inflow boundary is adjusted using an extrapolation from the inside (downstream). Since the flow is subsonic in the converging part of the nozzle, the pressure at the inflow boundary is eventually determined by the choked condition of the downstream nozzle.

3.2 *Law of the Wall*

In most cases, it is not practically feasible to use a sufficiently fine mesh to resolve thin boundary layers near walls. For turbulent flows, this difficulty can be circumvented by using the turbulent law of the wall. Compressibility effects on the turbulent law of the wall (Ref 21) are neglected in the present simulation because the error resulting from the relatively low Mach number (~1.5) is expected to be small. Implementation of the turbulent law of the wall for ordinary cells where solid walls coincide with cell faces was described previously (Ref 8). Here, a newly developed special treatment for "partial" cells is summarized.

A schematic of a typical partial cell is shown in Fig. 2. The cell faces are conveniently labeled as right (R), left (L), front (F), and derriere (D). The local velocity at the center of the mass (CM) is obtained as a weighted average of the cell face velocities.

$$\mathbf{u} = \frac{R_L u_L + R_R u_R}{R_L + R_R} \mathbf{i} + \frac{R_D v_D + R_F v_F}{R_D + R_F} \mathbf{j} \qquad \text{(Eq 23)}$$

where R_i is the R factor of the cell face i (i = R,L,F,D). The local Reynolds number can then be defined as $\text{Re} = \delta U/\nu$, where δ is the distance between the center of the mass of the cell and the wall. The magnitude of the shear stress then can be determined from (Ref 5):

$$\tau_w = \begin{cases} \rho U^2 / \text{Re} & (\text{Re} < 130.3) \\ \rho U^2 / (0.72 + 2.19 \ln \text{Re})^2 & (\text{Re} \geq 130.3) \end{cases} \qquad \text{(Eq 24)}$$

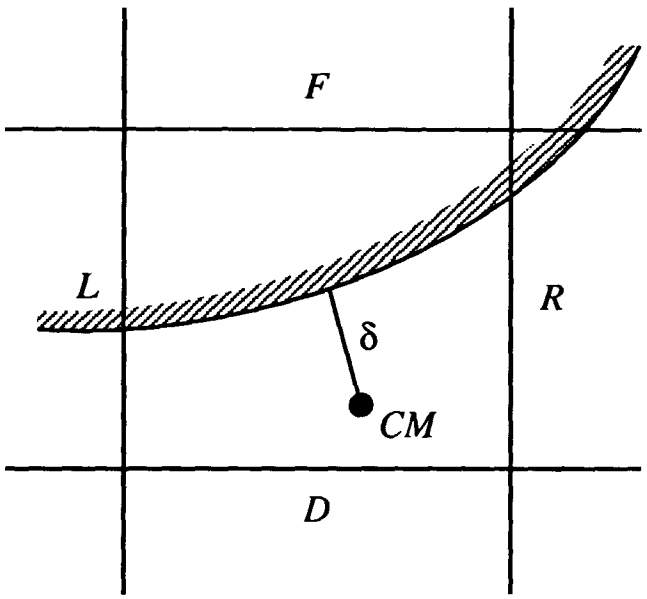

Fig. 2 Schematic of a partial cell to illustrate the "law of the wall." Refer to the text for further details.

The momentum change $\Delta\tilde{\mathbf{P}}$ is:

$$\Delta\tilde{\mathbf{P}} = \Delta\tilde{P}_{\parallel}\mathbf{t} = -\tau_w A_{\parallel}\Delta t\frac{U}{|U|}\mathbf{t} \quad \text{(Eq 25)}$$

where $A_{\parallel}$ and $\Delta\tilde{P}_{\parallel}$, respectively, represent projected area (surface projected on the parallel plane) and explicit change of parallel momentum.

It is desirable to add this explicit momentum change to the cell momentum in an implicit manner for numerical stability, which can be accomplished by writing:

$$P_{\parallel}^{n+1} - \tilde{P}_{\parallel} = \Delta\tilde{P}_{\parallel}\frac{P_{\parallel}^{n+1}}{\tilde{P}_{\parallel}} \quad \text{(Eq 26)}$$

where $\tilde{P}_{\parallel}$ represents the parallel component of the partially updated momentum due to convection and diffusion. The actual momentum change added to the cell momentum is then:

$$\Delta\mathbf{P} = -\frac{\Delta\tilde{\mathbf{P}}}{1 - \Delta\tilde{P}_{\parallel}/P_{\parallel}} = \Delta P_x\mathbf{i} + \Delta P_y\mathbf{j} \quad \text{(Eq 27)}$$

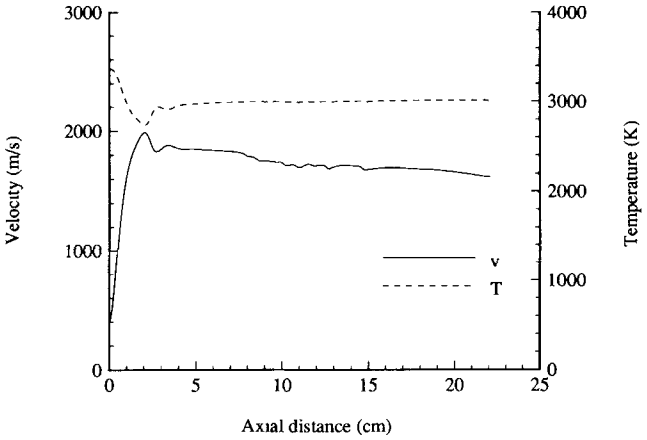

Fig. 3 Axial velocity (v) and temperature (T) of gas along the centerline

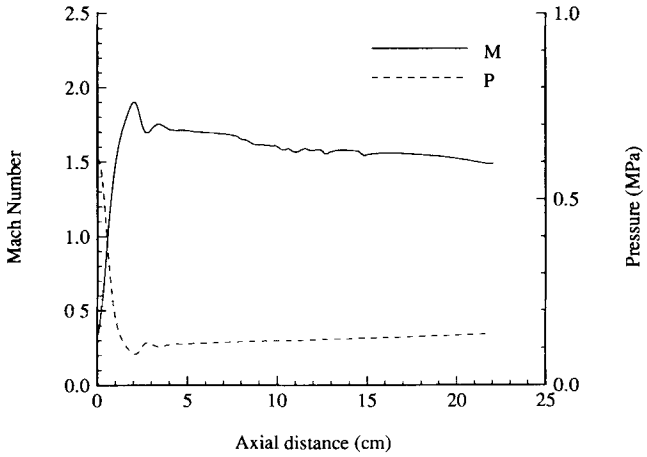

Fig. 4 Mach number (M) and pressure (p) along the centerline

where $P_{\parallel}$ is the parallel component of the old-time cell momentum. The x and y components of $\Delta\mathbf{P}$, ΔP_x, and ΔP_y are then distributed to the corresponding momentum cells according to:

$$\Delta\mathbf{P} = \frac{R_L\Delta P_{xL} + R_R\Delta P_{xR}}{R_L + R_R}\mathbf{i} + \frac{R_D\Delta P_{yD} + R_F\Delta P_{yF}}{R_D + R_F}\mathbf{j} \quad \text{(Eq 28)}$$

Using the Reynolds analogy, the thermal boundary layer can be treated in the same way. The resulting heat flux is:

$$\mathbf{q}_w = \frac{K}{\mu}\left(\frac{\tau_w}{|U|}\right)(T - T_w) \quad \text{(Eq 29)}$$

Even though there is no net mass flux to the wall, species diffusion fluxes to the wall are nonzero due to chemical reactions at the walls; e.g., wall recombination. By applying the Reynolds analogy for mass transfer, the diffusion mass flux of species i to the wall can be written as (Ref 8):

$$\mathbf{J}_i = \frac{cM_iD_i}{\mu}\left(\frac{\tau_w}{|U|}\right)(x_i - x_{iw}) \quad \text{(Eq 30)}$$

where D_i and x_i are the molecular effective binary diffusion coefficient (Ref 7, 15) and mole fraction of species i, respectively, and x_{iw} is the equilibrium mole fraction of species i at the wall temperature, assuming fully catalytic walls.

The fluxes given by Eq 30 will not satisfy the requirement of zero total mass flux at the wall (Ref 15). This problem can be solved by regarding the fluxes of Eq 30 as the precorrected diffusion fluxes described in Ref 15, to which the effective binary diffusion corrections (Ref 15) are then applied. In this way, species diffusion to the wall is calculated self-consistently. The heat flux to the wall is then the sum of the heat flux $\mathbf{J}$ and the chemical energy flux implied by the diffusion fluxes.

It also is necessary to allow for kinetic energy dissipated by the wall friction. The kinetic energy dissipated by wall friction in each cell on each time step is approximated by:

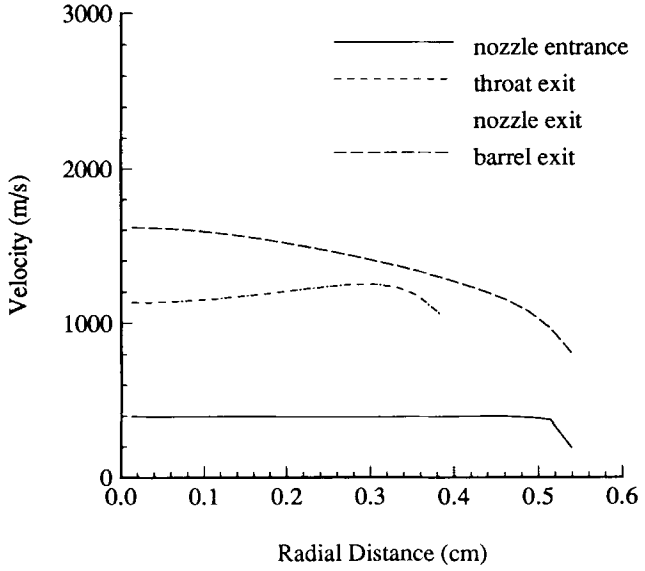

Fig. 5 Radial profiles of axial velocities at different axial locations

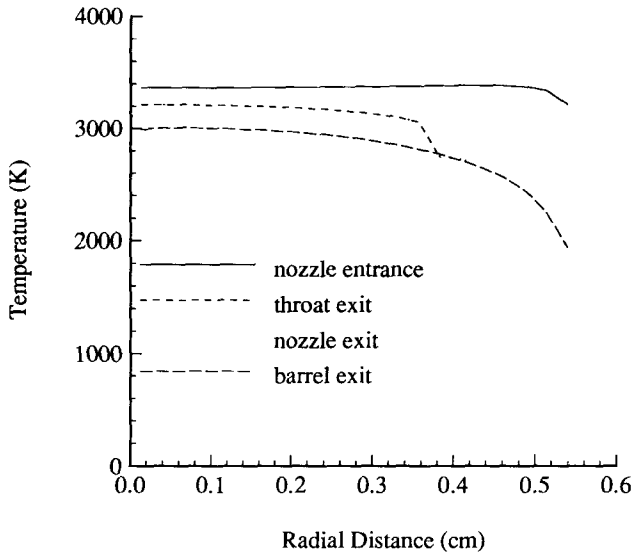

Fig. 6 Radial temperature profiles at different axial locations

$$\Delta k = -\frac{\Delta E}{M_c} = \frac{1}{2M_c^2}\left(|\tilde{\mathbf{P}}|^2 - |\mathbf{P}^{n+1}|^2\right) = \frac{1}{2M_c^2}\left(|\tilde{P}_{\parallel}|^2 - |P_{\parallel}^{n+1}|^2\right) \quad \text{(Eq 31)}$$

The boundary condition for the turbulent energy dissipation rate ε is (Ref 6):

$$\varepsilon = \frac{c_\mu^{3/4} k^{3/2}}{\kappa\delta} \quad \text{(Eq 32)}$$

where $\kappa = 0.4$ (Ref 22).

4. Computational Results

The model described above has been applied to simulate HVOF spraying of Inconel particles. The particles were injected into the turbulent combustion products flowing through the torch barrel. Typical operating conditions of a commercial torch (Hobart-Tafa JP-5000) were used: fuel mass flow rate $\dot{M}_{\text{fuel}}$ = 4.5 g/s and oxygen mass flow rate $\dot{M}_{O_2}$ = 15.44 g/s (Ref 20). The loading rate of Inconel 718 is 65 g/min (Ref 4). The particle size ranges from 15 to 63 μ in diameter, and the distribution is from Ref 4. Particles are continuously generated and injected into the flow. The injection velocity is uniformly distributed between 7 and 13 m/s in magnitude and within a 30 degree spray angle in direction. A typical computational particle contains approximately 15 physical particles. The surface emissivity of Inconel was 0.4

The calculation was first run to steady state in the absence of particles. The resulting solution served as the initial condition (t = 0) for the transient particle spraying simulation. Particles are injected from a ring injector to maintain axisymmetry. A statistically steady solution is obtained as the long-term limit of the transient calculation.

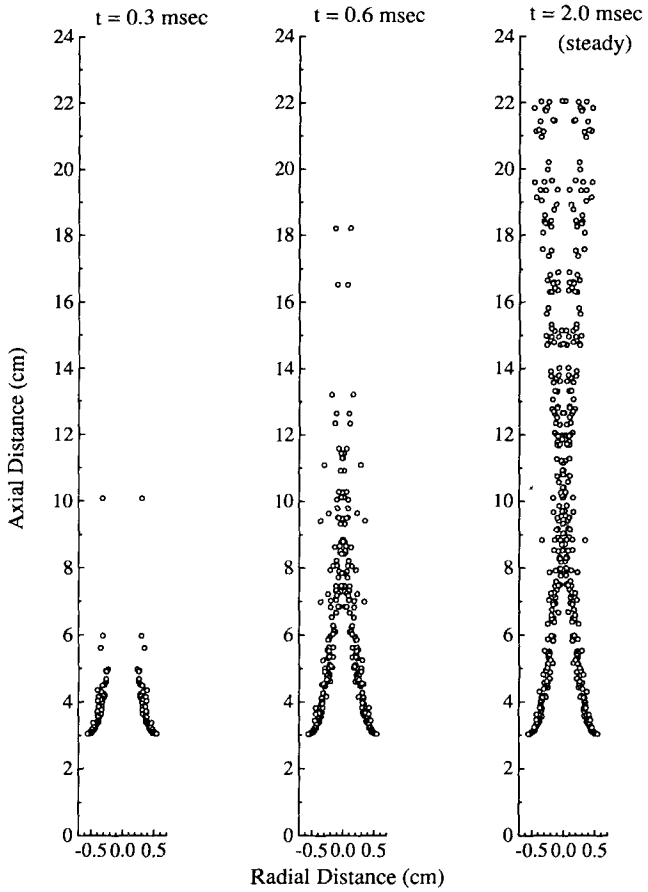

Fig. 7 Computational particles at different times (the nozzle exit is ~22 cm)

Figure 3 shows the gas velocity and temperature along the centerline at the statistically steady state with particles (t = 2 ms). Plots at steady state in the absence of the particles are not presented because the differences are small and visually indistinguishable. Swank et al. (Ref 4) reported that particle velocity and temperature do not depend on the loading rate up to 80 g/min. This indicates that the particles have little effect on the gas flow up to that loading rate, consistent with our calculated results, and that the previous work neglecting gas-particle interactions (Ref 3) is valid up to that loading rate. However, our approach with fully consistent gas-particle interactions is expected to be necessary in cases with heavier particle loading rates, where gas-particle interactions can be significant.

Figures 3 and 4 show that the gas temperature and pressure slightly increase in the barrel due to the recovery of kinetic energy, even though the gas flow is losing its energy due to wall cooling. Note that the Mach number in Fig. 4 is based on the frozen speed of sound.

Figures 5 and 6 show radial profiles of axial velocity and temperature at various axial locations. Again, the velocity decreases from the nozzle exit to the barrel exit, while temperature increases due to the recovery effect. The calculated axial velocity and temperature agree quite well with the experimental values (Ref 20).

Figure 7 shows the computational particles in the computational region at different times during the transient. The particle

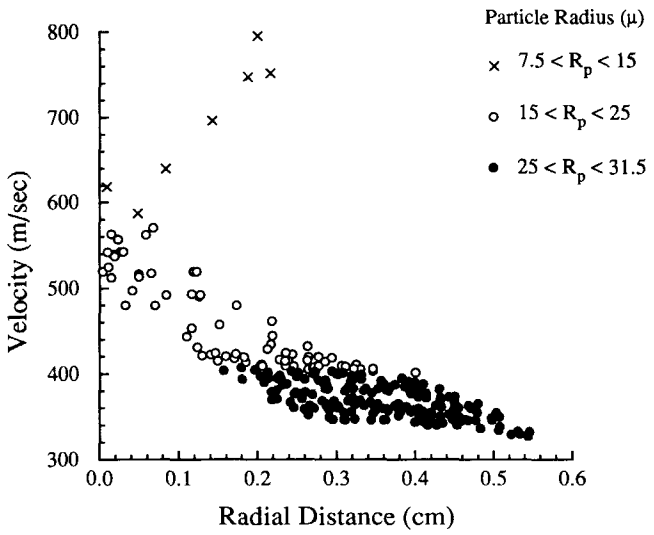

Fig. 8 Particle axial velocity distribution at the exit of the torch at $t = 2$ ms

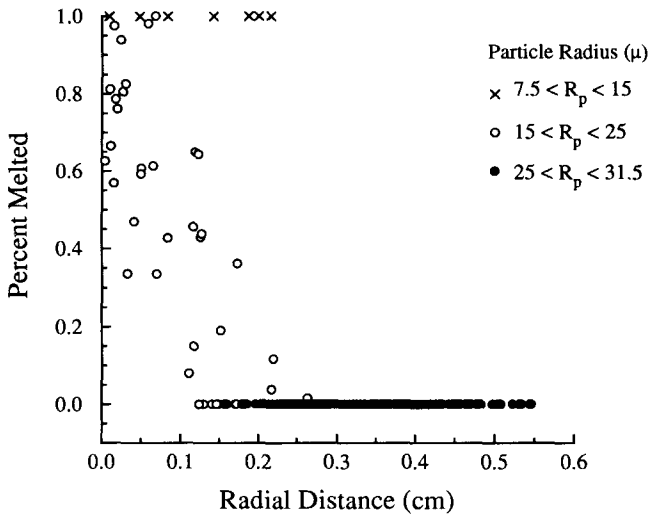

Fig. 10 Particle degree-of-melting distribution at the exit of the torch at $t = 2$ ms

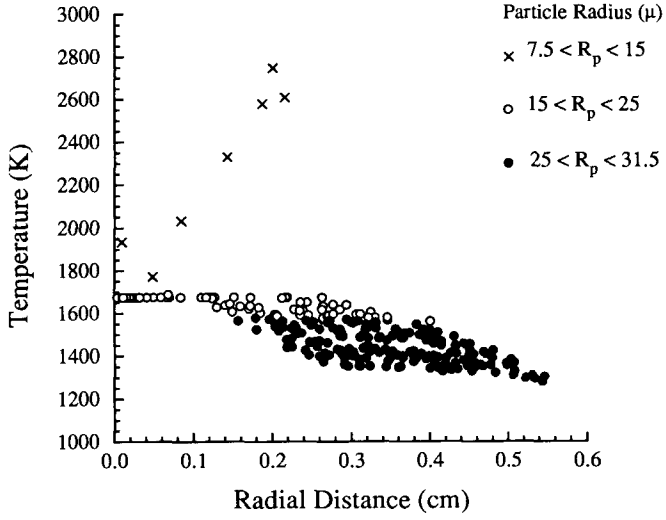

Fig. 9 Particle temperature distribution at the exit of the torch at $t = 2$ ms

spray pattern has reached a statistically steady state by $t = 2$ ms. However, slightly different spray patterns will be obtained at different times in the statistically steady state. Figures 8 and 9 show the particle velocity and temperature distributions at the nozzle exit. These statistical distributions were collected during the interval 1 ms $< t <$ 2 ms during the statistical steady state. The overall results show quite good agreement with the experimental results where particle velocities range between 420 and 520 m/s. Notice that the particle spray pattern at this axial distance is hollow cone because most particles cross the axis and continue to move away from it. This spray pattern resulted from the 2-D simulation and ring injection. Particle size distribution, shown in Fig. 8 and 9, indicates that particle acceleration and heating strongly depend on the particle size.

The calculated particle temperature distribution is shown in Fig. 9. The calculated particle temperatures tend to be higher than the experimental results, which range from 1100 to 1300 K. We suspect that these errors result from the 2-D simulation, in which all particles pass through the axis where the gas temperature is high. In reality, most particles probably do not pass through the axis, resulting in a 3-D spray situation. Nevertheless, the results show relatively good agreement with the experimental results because the gas temperature distribution in the barrel is relatively uniform as shown in Fig. 6. The calculated particle degree-of-melting distribution is shown in Fig. 10. Most particles did not reach the melting temperature, as shown in Fig. 9. Figure 10 shows that particles are only partially molten even at the melting temperature. Again, particle heating and melting strongly depend on the particle size.

Figure 11 shows the particle size distribution. Figure 11, combined with Fig. 8 and 9, shows that smaller particles have higher velocities and higher temperatures as expected. Figure 11 also shows that heavier (larger) particles penetrate further into the gas due to their larger mass and momentum.

5. Concluding Remarks

We assumed that the combustion process is complete in the combustion chamber. This assumption may be responsible for the fact that the calculated gas and particle temperatures are slightly higher than the experimental results. A complete simulation of spray combustion in the combustion chamber may be necessary, and we hope to include that in a future study.

The 2-D particle spray simulation is also expected to produce higher particle velocities and temperatures because particles pass through the symmetry axis where the gas velocity and temperature are high. However, the calculated results still show relatively good agreement with the experimental results due to the relatively uniform gas flow field in the barrel. Three-dimensional studies may be necessary for heavier particle loading rates or different torch geometries.

In summary, we presented a fully consistent numerical simulation of HVOF spraying with injected particles. The transient

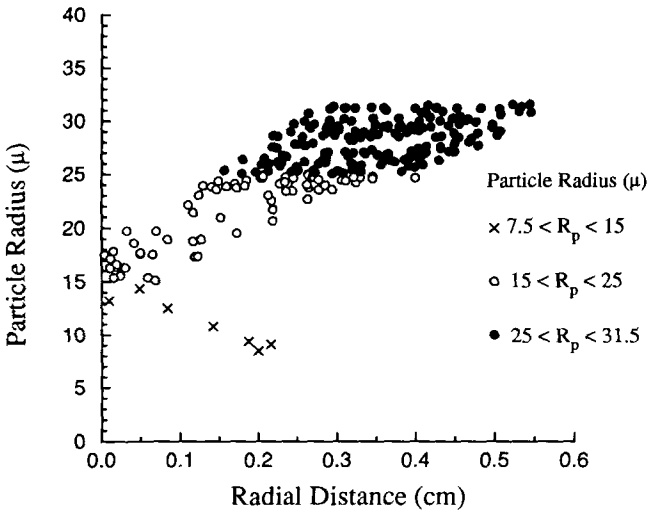

Fig. 11 Particle size distribution at the exit of the torch at t = 2 ms

solution using the stochastic particle model provides important insights into the statistical variations in particle temperature, velocity, size, and degree of melting. These results are expected to play an important role in achieving better understanding and optimization of the HVOF process.

Acknowledgments

We would like to express our gratitude to J.D. Ramshaw, J.R. Fincke, and W.D. Swank for helpful discussions. This work was performed under the auspices of the U.S. Department of Energy under DOE Field Office, Idaho, contract DE-AC07-94ID13223, supported by the INEL Laboratory Directed Research and Development program and in part by the INEL Long Term Research Initiative in Computational Mechanics. The development of the LAVA computer code was supported by the Division of Engineering and Geosciences, Office of Basic Energy Sciences, DOE-OER.

References

1. M.L. Thorpe and H.J. Richter, A Pragmatic Analysis and Comparison of the HVOF process, *Thermal Spray: International Advances in Coatings Technology*, C.C. Berndt, Ed., ASM International, 1992, p 137-147
2. G.D. Power, T.J. Barber, and L.M. Chiappetta, Analysis of a High Velocity Oxygen-Fuel (HVOF) Thermal Torch, *AIAA/SAE/ASME/ASEE 28th Joint Propulsion Conference and Exhibit* (Nashville, TN), AIAA paper 92-3598, 1992
3. E.B. Smith, G.D. Power, T.J. Barber, and L.M. Chiappetta, Application of Computational Fluid Dynamics to the HVOF Thermal Spray Gun, *Thermal Spray: International Advances in Coatings Technology*, C.C. Berndt, Ed., ASM International, 1992, p 805-810
4. W.D. Swank, J.R. Fincke, D.C. Haggard, G. Irons, and R. Bullock, HVOF Particle Flow Field Characteristics, *Thermal Spray Industrial Applications*, C.C. Berndt and S. Sampath, Ed., ASM International, 1994, p 319-324
5. A.A. Amsden, J.D. Ramshaw, P.J. O'Rourke, and J.K. Dukowicz, "KIVA: A Computer Program for Two- and Three-Dimensional Fluid Flows with Chemical Reactions and Fuel Sprays," Report LA-10245-MS, Los Alamos National Laboratory, Feb 1985
6. A.A. Amsden, P.J. O'Rourke, and T.D. Butler, "KIVA-II: A Computer Program for Chemically Reactive Flows and Fuel Sprays," Report LA-11560-MS, Los Alamos National Laboratory, May 1989
7. J.D. Ramshaw and C.H. Chang, Computational Fluid Dynamics Modeling of Multicomponent Thermal Plasmas, *Plasma Chem. Plasma Process.*, Vol 12, 1992, p 299-325
8. C.H. Chang, Numerical Simulation of Alumina Spraying in an Argon-Helium Plasma Jet, *Thermal Spray: International Advances in Coatings Technology*, C.C. Berndt, Ed., ASM International, 1992, p 793-798
9. C.H. Chang and J.D. Ramshaw, Numerical Simulations of Argon Plasma Jets Flowing into Cold Air, *Plasma Chem. Plasma Process.*, Vol 13, 1993, p 189-209
10. J.R. Fincke, C H. Chang, W.D. Swank, and D.C. Haggard, Entrainment and Demixing in Subsonic Thermal Plasma Jets: Comparison of Measurements and Predictions, *Int. J. Heat Mass Transfer*, Vol 37, 1994, p 1673-1682
11. C.H. Chang and J.D. Ramshaw, Numerical Simulation of Nonequilibrium Effects in an Argon Plasma Jet, *Phys. Plasmas*, Vol 1, 1994, p 3698-3708
12. R.A. Gentry, R.E. Martin, and B.J. Daly, An Eulerian Differencing Method for Unsteady Compressible Flow Problems, *J. Comput. Phys.*, Vol 1, 1966, p 87-118
13. J.D. Ramshaw and J.K. Dukowicz, "APACHE: A Generalized-Mesh Eulerian Computer Code for Multicomponent Chemically Reactive Fluid Flow," Report LA-7427, Los Alamos Scientific Laboratory, Jan 1979
14. C.H. Chang and J.D. Ramshaw, Numerical Simulation of High-Speed Plasma Flow Past an Enthalpy Probe, *Plasma Chem. Plasma Process.*, in press
15. J.D. Ramshaw, Self-Consistent Effective Binary Diffusion in Multicomponent Gas Mixtures, *J. Non-Equilib. Thermodyn.*, Vol 15, 1990, p 295-300
16. S. Gordon and B.J. McBride, "Computer Program for Calculation of Complex Chemical Equilibrium Compositions, Rocket Performance, Incident and Reflected Shocks, and Chapmann-Jouguet Detonations," NASA SP-273, Vol 1, National Aeronautics and Space Administration, 1976, p 1
17. J.D. Ramshaw and C.H. Chang, "Iteration Scheme for Implicit Calculations of Kinetic and Equilibrium Chemical Reactions in Fluid Dynamics," *J. Comput. Phys.*, Vol 116, 1995, p 359-364
18. E. Gutheil, G. Balakrishnan, and F.A. Williams, Structure and Extinction of Hydrogen-Air Diffusion Flames, *Reduced Kinetics Mechanisms for Applications in Combustion Systems*, N. Peters and B. Rogg, Ed., Springer-Verlag, 1993
19. M. Slack and A. Grillo, High Temperature Rate Coefficient Measurements of CO + O Chemiluminescence, *Combust. Flame*, Vol 59, 1985, p 189-196
20. W.D. Swank, J.R. Fincke, D.C. Haggard, and G. Irons, HVOF Gas Flow Characteristics, *Thermal Spray Industrial Applications*, C.C. Berndt and S. Sampath, Ed., ASM International, 1994, p 313-318
21. E.J. Hopkins and M. Inouye, An Evaluation of Theories for Predicting Turbulent Skin Friction and Heat Transfer on Flat Plates at Supersonic and Hypersonic Mach Numbers, *AIAA J.*, Vol 9, 1971, p 993-1003
22. H. Schlichting, *Boundary Layer Theory*, McGraw-Hill, 1979